Interatomic potentials for modelling radiation defects and dislocations in tungsten

2013 J. Phys.: Condens. Matter 25 395502

(http://iopscience.iop.org/0953-8984/25/39/395502)

IOP PUBLISHING JOURNAL OF PHYSICS: CONDENSED MATTER

J. Phys.: Condens. Matter **25** (2013) 395502 (15pp) doi:10.1088/0953-8984/25/39/395502

Interatomic potentials for modelling radiation defects and dislocations in tungsten

M-C Marinica[1], Lisa Ventelon[1], M R Gilbert[2], L Proville[1], S L Dudarev[2], J Marian[3], G Bencteux[4] and F Willaime[1]

[1] CEA, DEN, Service de Recherches de Métallurgie Physique, F-91191 Gif-sur-Yvette, France
[2] EURATOM/CCFE Fusion Association, Culham Centre for Fusion Energy, Abingdon, Oxfordshire OX14 3DB, UK
[3] Lawrence Livermore National Laboratory, Livermore, CA 94551, USA
[4] EDF-R&D SINETICS, 1 avenue du Général de Gaulle, F-92141 Clamart Cedex, France

E-mail: mihai-cosmin.marinica@cea.fr

Received 15 April 2013, in final form 25 June 2013
Published 4 September 2013
Online at stacks.iop.org/JPhysCM/25/395502

Abstract

We have developed empirical interatomic potentials for studying radiation defects and dislocations in tungsten. The potentials use the embedded atom method formalism and are fitted to a mixed database, containing various experimentally measured properties of tungsten and *ab initio* formation energies of defects, as well as *ab initio* interatomic forces computed for random liquid configurations. The availability of data on atomic force fields proves critical for the development of the new potentials. Several point and extended defect configurations were used to test the transferability of the potentials. The trends predicted for the Peierls barrier of the $\frac{1}{2}\langle 111\rangle$ screw dislocation are in qualitative agreement with *ab initio* calculations, enabling quantitative comparison of the predicted kink-pair formation energies with experimental data.

(Some figures may appear in colour only in the online journal)

1. Introduction

Progress in fusion and advanced fission power generation technology depends critically on the development of new high temperature materials. Tungsten alloys appear to be promising candidates for the challenging fusion environment, although the question of stability of these alloys under high energy neutron irradiation remains largely unexplored. In metal alloys, including tungsten alloys, microstructural evolution occurring under irradiation is strongly dependent on the properties of point defects, such as interstitial atoms and vacancies, and also on the properties of extended defects, such as dislocations and surfaces.

In order to establish a link between processes occurring at microstructural and atomic levels, large-scale discrete atomistic simulations are required. The latter necessitates using simulation cell sizes that in most cases, especially for extended defects, are not readily accessible to *ab initio* calculations. In this context, the availability of sufficiently accurate interatomic potentials proves pivotal since simulations performed using such potentials can model systems containing millions of atoms.

The characteristic feature of large-scale atomistic simulations is a simple approximate treatment of interatomic bonding. By using an interatomic potential, the energy of bonding between atoms is expressed solely as a function of atomic coordinates, with the electronic degrees of freedom included only implicitly. For example, in metals where the shape of the electronic density of states (DOS) is relatively simple, the embedded atom method (EAM) potentials [1–3] are valid and successfully and widely applied. The energy of an atomic system in the EAM formalism is given by the sum of pair potential terms, which include the shielded Coulomb repulsion between the nuclei, and the

embedding energy term describing the formation of collective chemical bonds between the neighbouring atoms. These potentials are particularly well suited for modelling simple or noble metals with face-centred cubic (FCC) or hexagonal close-packed (HCP) structure [1, 4–6], and can also be successfully applied to body-centred cubic (BCC) metals [3, 7]. In BCC transition metals, such as tungsten (W), where the d band is only partially filled, there is evidence that d bonds have angular character. Hence EAM may be augmented with angular terms, as in Baskes' modified EAM (MEAM) [8], or even supplemented by a more accurate DOS description, such as that given by the tight-binding method [9] and its computationally more efficient version, the bond order potential (BOP) [10, 11]. The BOP formalism has been developed over the last 20 years, and there are parametrizations available for several transition metals including Fe, W, and Mo [12–15]. However, due to their simplicity and numerical efficiency, EAM potentials remain the tool of choice for the great majority of finite temperature molecular dynamics simulations.

The performance and transferability of the EAM potentials is not only related to the physical model underpinning the embedded atom model, but also to the observable properties chosen for the optimization of the functional form and numerical parameters defining a potential [7, 16–18]. Reasonably accurate potentials are developed using large fitting databases, which contain experimentally measured quantities as well as the data derived from *ab initio* methods, such as the total energies and forces acting on atoms in various configurations. This latter idea stimulated Ercolessi and Adams to develop the force-matching method (FMM) [16], where it was observed that the choice of the database used for fitting a potential was as significant as the choice of approximation for the electronic structure effects. For this reason, EAM potentials are mostly valid when used to simulate configurations not very dissimilar to those used in the fitting procedure. The comparatively poor transferability of EAM potentials is the price that one has to pay for the relative simplicity of the formalism.

Mendelev *et al* [19–21] developed several different EAM potentials for BCC Fe, a metal which is known to be more complex than W because of its magnetic properties. In these potentials, the EAM Finnis–Sinclair functional form of the embedding function, where the attractive interaction between atoms is assumed to be proportional to the square root of the local electron density [3], is augmented by a polynomial function, describing electron correlation effects. Mendelev *et al* [19] showed that a fit performed using the Ercolessi and Adams FMM [16] produced reasonable values for the formation energies of interstitial defects. However, the deviation from the results of first-principles calculations remained substantial. Recently, using the same fitting approach and a larger *ab initio* database, Marinica *et al* [22] derived a potential that gave an improved description of point defects. Meanwhile, in 2005 Dudarev and Derlet [23] followed an alternative approach to develop a 'magnetic' potential based on the EAM formalism, where the embedding part of the potential was derived using a combination of the Stoner and Landau models. By systematically enlarging the fitting databases, the magnetic potentials were continuously improved [24, 25]. However, despite their lower accuracy, in comparison with Marinica [22] and Dudarev–Derlet [23] potentials, in describing the energy landscape of point defects, Mendelev's potentials [19–21] have remained, until recently, the reference models for the study of screw dislocations in iron. In particular, the 2003 Mendelev potential (version 2) predicts the following characteristic properties of screw dislocations in iron [21]: (i) a compact non-degenerate dislocation core, in agreement with *ab initio* calculations; (ii) a Peierls potential barrier with two maxima separated by a pronounced minimum at the halfway position [26], which is different from the case for *ab initio* calculations where only one maximum is observed [27], and the DFT barrier is also four times higher; and (iii) a {110} glide plane, in agreement with experiment and *ab initio* calculations [28]. Recently, Proville *et al* [29] proposed a potential that improves the description of the Peierls potential, by eliminating the double-humped shape of the barrier and leading to a more robust {110} glide plane.

The fitting procedure used for developing all of the above potentials was broadly the same: a potential was fitted to a database containing several experimentally measured quantities (elastic constants, cohesive energies, surface energies, etc), using FMM applied to several atomic configurations, and the database also included some of the minimum energy configurations of point defects, for example those representing self-interstitial atom defects and vacancies. We note one aspect of Mendelev's [19–21] and Proville's [29] fitting procedures that distinguishes them from the approaches used by other authors: the use of FMM involving liquid far-from-equilibrium atomic configurations. The *ab initio* data on liquid configurations appear to play an important role in ensuring the correct properties of extended defects and dislocations predicted by simulations.

As opposed to the case for BCC iron, there are very few EAM potentials in the literature suitable for modelling W. The first many-body potential for tungsten, together with other BCC metals, was proposed by Finnis and Sinclair [3] (hereafter this potential will be referred to as the FS potential). All of the FS potentials are tight-binding second-moment potentials, short-range (the cut-off between the second-neighbour and third-neighbour shells), and fitted to fundamental bulk properties. Ackland and Thetford [7] subsequently noted that the FS potentials, particularly those for tungsten, do not correctly describe the self-interstitial atom defect configurations where separations between some of the atoms are fairly small. Consequently, Ackland and Thetford enlarged the fitting database and included in the fit the electron gas calculation of the W short-distance dimer properties (here we refer to the Ackland and Thetford potential as the AT potential). This potential was used in the community for a wide range of applications, from bulk related properties to radiation damage simulations or the energy landscape of point defects and dislocations in W. For instance the seminal work of Duesbery and Vitek [30] is one of the first atomistic simulations using a many-body potential, namely AT, in order

to explore the energy landscape of screw dislocations in BCC metals. Recently, modifying the short-range part of the AT potential (for distances lower than the nearest-neighbour distances in the pairwise part), Juslin and Wirth [31] proposed a new parametrization of the interatomic potential for W. They used the new potential to investigate helium-vacancy clustering in tungsten.

Wang *et al* [32] developed potentials for all the BCC metals that were designed to properly describe the phonon spectra. They showed that having a longer-range pairwise part of an EAM potential (with the cut-off between the fifth and sixth neighbours), combined with a suitable choice of the embedding part, increased its ability to describe the phonon anomalies of BCC metals. However, these potentials poorly describe the energy landscape of point defects in finite temperature simulations.

Using, as a starting point, the family of short-range FS-type potentials, Derlet *et al* [33] found new parametrizations for vanadium, niobium, tantalum, molybdenum, and tungsten. The fitting database was significantly enlarged to include *ab initio* point defect formation energies corresponding to relaxed mono-vacancy and self-interstitial atom configurations. These potentials were then used to investigate the thermally activated migration of self-interstitial atom defects in tungsten [33, 34]. Despite some deficiencies, such as the incorrectly predicted degenerate core for screw dislocations, the new W potential represented an improvement compared to those available previously.

In this paper we follow a fitting procedure similar to that applied by Mendelev *et al* [19–21] and Proville *et al* [29] to iron, and produce a new set of empirical potentials for tungsten. Specifically, we use FMM to parametrize the EAM potentials. Our goal is to develop new potentials for tungsten that would agree with *ab initio* simulations of radiation defects and dislocations. Section 2 describes the key stages of the fitting procedure. The transferability of fits with respect to point and extended defects is then assessed in the subsequent sections of the paper. Conclusions are presented in section 5 and finally the parametrizations of the potentials are given in the appendix.

2. Development of an EAM potential for W

The analytical form of EAM potentials adopted in this work is the same as in the model developed by Mendelev [20] and Ackland *et al* for iron [19]. This form is given below:

$$E\left(\mathbf{r_1},\ldots,\mathbf{r_N}\right)=\sum_{i=1}^{N}\left[\sum_{j>i}^{N}\Phi\left(r_{ij}\right)+F\left(\rho_{\mathrm{i}}\right)\right], \tag{1}$$

$$\Phi\left(x\right)=\sum_{i=1}^{n^{\Phi}}a_{\mathrm{i}}^{\Phi}\left(\delta_{\mathrm{i}}^{\Phi}-x\right)^{3}\Theta\left(\delta_{\mathrm{i}}^{\Phi}-x\right), \tag{2}$$

$$\rho\left(x\right)=\sum_{i=1}^{n^{\rho}}a_{\mathrm{i}}^{\rho}\left(\delta_{\mathrm{i}}^{\rho}-x\right)^{3}\Theta\left(\delta_{\mathrm{i}}^{\rho}-x\right), \tag{3}$$

$$F\left(x\right)=a_1^F\sqrt{x}+a_2^Fx^2. \tag{4}$$

Here Φ, ρ and F are the functions describing pairwise interatomic interactions, the effective electron density, and the collective d electron embedded function, respectively. $\Theta(x)$ is the Heaviside step function, equal to 1 for $x \geq 0$ and 0 otherwise. In the fitting process we search for the best set of parameters $\mathbf{A}=(a_1^{\Phi},\ldots,a_{n^{\Phi}}^{\Phi};a_1^{\rho},\ldots,a_{n^{\rho}}^{\rho};a_1^F,a_2^F)$. Once it is specified, the positions of the cubic spline knots $(\delta_1^{\Phi},\ldots,\delta_{n^{\Phi}}^{\Phi};\delta_1^{\rho},\ldots,\delta_{n^{\rho}}^{\rho})$ are adjusted to further improve the fit.

The fitting procedure is based on the principle of variational assimilation [35, 36]. For various sets of parameters $\mathbf{A}$, the results obtained with the corresponding EAM model are compared with the database and an objective function characterizing the deviation is minimized. For a given set of parameters $\mathbf{A}$, the objective function has the form

$$J\left(\mathbf{A}\right)=\sum_{\mathrm{obs}}w_{\mathrm{obs}}\left[\mathbf{Y}_{\mathrm{obs}}-\mathbf{Y}_{\mathrm{obs}}(\mathbf{A})\right]^2+\sum_{\mathrm{i}}w_{\mathrm{i}}\left[\mathbf{F}^i_{ab\ initio}-\mathbf{F}^i(\mathbf{A})\right]^2. \tag{5}$$

Variable $\mathbf{Y}_{\mathrm{obs}}$ represents the database values and $\mathbf{Y}_{\mathrm{obs}}(\mathbf{A})$ are the corresponding values computed using a set of parameters $\mathbf{A}$ and the corresponding EAM potential defined by equation (1). Variable $\mathbf{F}^i_{ab\ initio}$ represents the target *ab initio* forces and $\mathbf{F}^i(\mathbf{A})$ is the force acting on atom i, computed using the EAM potential with parameters $\mathbf{A}$. Coefficients w are the weights defined by the user—the choice of which will be discussed later. Fitting is performed using the ASSIMPOT code [37, 38].

The objective function $J(\mathbf{A})$ is minimized using an iterative algorithm. We start with an initial set of parameters $\mathbf{A}$ and at each iteration step an improved vector of parameters is sought. The search direction is computed from the gradient of the objective function with respect to the vector of parameters. The gradient is computed within the adjoint model [35, 36] to avoid the numerical instabilities associated with the nonlinear character of the objective function. Alternatively, the gradient vector could be approximated by finite differences, although the adjoint model has the advantage of having higher precision and better computational efficiency.

2.1. The database used for fitting the potential parameters

The database contains data of three types:

(i) Experimentally measured values of solid state properties: lattice parameters and cohesive energies of BCC structure, and elastic constants C_{11}, C_{12} and C_{44}. We have included in the fit the FCC cohesive energy which has been fixed as the difference between the BCC and FCC cohesive energies computed using an *ab initio* technique (described below) and the experimental BCC cohesive energy.

(ii) *Ab initio* formation energies computed for basic point defects in tungsten: a mono-self-interstitial atom with different crystallographic orientations, i.e. ⟨110⟩, ⟨111⟩, ⟨100⟩, and locations in the unit cell, i.e. octahedral and tetrahedral; and a mono-vacancy. The *ab initio*

Table 1. Target values of properties to which the four EAM potentials were fitted, and the values computed using the potentials: lattice parameters (a_0) and cohesive energies (E_{coh}) of the BCC and FCC structures, elastic constants (C_{11}, C_{12} and C_{44}), and the formation energies E_f of a mono-vacancy and self-interstitial atom defects with different orientations. The formation energies for a mono-interstitial and a mono-vacancy were computed using each EAM potential for a supercell with 128 ± 1 atoms (i.e. we used the same simulation box as was used in the fitting process and the SIESTA GGA calculations). The cohesive energy of the FCC structure is computed by adding to the experimental value of E_{coh} for the BCC phase the DFT GGA difference between the energies of the BCC and FCC structures.

	Target Value	Potential EAM1	Potential EAM2	Potential EAM3	Potential EAM4
			Bulk properties		
a_0 BCC (Å)	3.1648[a]	3.185 82	3.140 00	3.187 37	3.143 39
a_0 FCC (Å)	4.054[b]	4.013 54	4.053 44	4.199 49	4.053 42
E_{coh} BCC (eV/atom)	−8.9[a]	−8.900 3	−8.899 98	−8.900 1	−8.899 97
E_{coh} FCC (eV/atom)	−8.43[b]	−8.410 2	−8.429 99	−8.445 6	−8.430 00
C_{11} (GPa)	523[a]	523	544	519	523
C_{12} (GPa)	203[a]	203	208	203	202
C_{44} (GPa)	160[a]	160	160	159	161
			Defect properties		
$E_f^{\langle 111\rangle}$ (eV)	10.53[b]	10.53	10.52	10.53	10.53
$E_f^{\langle 110\rangle}$ (eV)	10.82[b]	10.83	10.82	10.95	10.82
$E_f^{\langle 100\rangle}$ (eV)	12.87[b]	12.89	12.86	11.18	12.72
E_f^{OCT} (eV)	13.11[b]	13.16	12.64	10.99	12.52
E_f^{TET} (eV)	12.27[b]	12.27	11.94	11.74	11.87
E_f^V (eV)	3.49[b]	3.59	3.49	4.38	3.81

[a] Values taken from Landolt–Börnstein [45].

[b] Values computed using the SIESTA GGA code [42].

values were obtained from calculations performed within the density functional theory (DFT) framework using the SIESTA code [39] in the norm-conserving pseudopotential approximation for localized basis sets—constructed from 15 localized functions [42, 51]. The 6s, 6p and 5d states for tungsten were treated as valence, and 5s and 5p orbitals were not included in the valence band. The defect calculations were performed using the supercell approximation, keeping the cell geometry fixed to the bulk equilibrium geometry and relaxing the atomic positions. The 4^3 shifted k-point grid was used for the 128-atom cell. The Hermite–Gauss scheme for the electronic density of state broadening was used with a smearing of 0.3 eV. Relaxations were terminated once the residual forces were smaller than 0.01 eV Å^{-1}. The Perdew–Burke–Ernzerhof generalized gradient approximation (GGA) was used for the exchange–correlation functional.

(iii) *Ab initio* forces acting on atoms in liquid (random) state configurations. All the configurations were generated using the Ackland–Mendelev [20] potential for iron. From the initial perfect BCC supercell with 128 atoms, 17 atoms were removed from random lattice sites in order to eventually obtain (after re-scaling the lattice parameter) the experimental liquid density of tungsten (1.67×10^4 kg m^{-3}). The system was evolved using molecular dynamics at 4000 K temperature over one million 1 fs time steps. From this molecular dynamics trajectory we extracted one liquid configuration every 50 ps. The time interval between snapshots was large enough to avoid correlations associated with the dynamic evolution of atomic system. Finally, the resulting set of twenty random configurations were re-scaled and used as input for *ab initio* calculation of forces acting between W atoms. The positions of atoms were fixed, and we computed only the atomic forces acting on each atom in each liquid configuration. The *ab initio* calculations were performed using SIESTA GGA with the same pseudopotentials and basis sets as were used for defect calculations.

The target values for the first two parts of the fitting database are given in the first column of table 1.

By including different *ab initio* liquid configurations in the database fitting, the resulting parametrizations of the potential contain information on the out-of-equilibrium (non-zero) forces. Moreover, the objective function, equation (5), is sampled through the pair and embedding part of the EAM potential on a continuous range of atom–atom interaction distances. On the other hand, in the case where only ordered atomic configurations are used in the database, the distribution of interatomic distances is discrete. For example in the case of a vacancy, the distribution of interaction distances is not very different from that characterizing a perfect crystal structure.

2.2. *The fitting procedure*

The starting point of the fitting procedure was the tungsten potential by Derlet *et al* [33], hereafter referred to as DNMD.

In the first step we extended the cut-off distance of the density part of the DNMD potential, $\rho(x)$ in equation (3), from a value corresponding to the second-neighbour atomic shell to a distance situated between the fourth and fifth neighbours. Note also that the density function $\rho(x)$ has a minimum knot of 2.5 Å (see the appendix), is unbounded at $x = 0$, and cannot be used below around 2 Å, and in any case the potentials described here should not be used to study configurations where the minimum interatomic distances are less than the minimum distances used in the fitting database (see below). The new density function was refitted using all the properties given in table 1. At this stage the typical choice of weights $w_{\rm obs}$ in the objective function, equation (5), is as follows: $w_{a_0} = 10\,000$ for the lattice parameter a_0 (which ensures that the database values are accurate up to four decimal places), $w_{E_{\rm coh}} = 1000$ for the cohesive energy, $w_{\rm c} = 1$ for elastic constants and $w_{\rm E} = 100$ for the energies of point defects.

The second stage is to fit the pairwise function Φ, equation (2), within five nearest-neighbour atomic shells. The positions of the cubic spline knots (parameters δ^{Φ}) were chosen on a grid that divides the distance between any two consecutive neighbour shells into four equal intervals. The knot points were assigned to each grid point except for those corresponding to the neighbour distances in a perfect BCC lattice, meaning that there were twelve knots in total. However, the smallest interatomic distance in the fitted configurations was 2.2 Å (only a little less than the distance between a pair of atoms in the centre of a W–W dumbbell), and so we added three supplementary knot points in order to fit these distances, which are smaller than the first-nearest-neighbour separation. Note that the potential parametrizations are not suitable for modelling configurations with minimum distances less than this 2.2 Å. Björkas *et al* [43] have recently shown how to successfully extend to short range the DNMD potential for W using the universal potential of Ziegler *et al* [44], and this will be subsequently repeated for the current potentials to make them appropriate for the study of high energy collision dynamics in cascades. The coefficients of the splines a^{Φ} and the two coefficients in the embedded part $a^{F}_{1,2}$ were randomly generated within a closed and bound interval of $[-500.0, 500.0]$. Several hundred fits were started with the same weights as in the first stage, and we selected ∼60 parametrizations which gave reasonably accurate target values in table 1. The liquid configurations were not included in the fit at this stage and only the zero-value forces corresponding to fully relaxed minimum energy point defect configurations were fitted.

At the third stage we proceed to iterative fitting of the three terms of the potential pair, density and embedded function, in order to obtain the values of fitted quantities closer to the target database values. In practice, one minimization of the objective function $J(\mathbf{A})$ is insufficient. It turns out that it is impossible to fit energies and forces simultaneously: if one relaxes the positions with one set of parameters $\mathbf{A}$ of the EAM potential, the relaxed energies deviate from their objective values. In other words, the DFT GGA and EAM force fields around the defects differ significantly. This type of fitting is therefore used only in the first and second stages. Subsequently, the atomic *positions* associated with the minimum energy configurations are those corresponding to fully atomically relaxed configurations found using the current version of the EAM potential. The fitting procedure is then iterated until convergence is achieved. Several converged sets of parameters were obtained using this methodology. It is interesting to note that at this stage of fitting, all of the fitted potentials predicted degenerate core structure for a screw dislocation, at variance with DFT calculations.

In the final stage we refine the parametrizations for the pairwise part of the potential, keeping the embedding part of the potential unchanged. At this stage we include in the fit the *ab initio* information about forces acting between the atoms in the liquid configurations. Using a weight of $w_{\rm i} = 0.1$ for these forces, we obtain a new class of potentials from which we select only those that have the correct non-degenerate core structure for the screw dislocation. A typical example is the EAM1 potential. Increasing the $w_{\rm i}$ weights to 1 and decreasing the w_E and w_{a_0} to 10 and 100, respectively, we obtain a second class of potentials, as exemplified by EAM2. A characteristic property of the second class of potentials is a reasonable shape for the Peierls potential barrier, which, in particular, is a single-humped profile in agreement with *ab initio* calculations, whereas for the potentials exemplified by EAM1 the Peierls barrier exhibits two saddle points with a pronounced minimum at the halfway position (the energy of which may be even lower than the initial energy of the screw dislocation in the easy core configuration). We conclude that the force-matching method that uses *ab initio* information about liquid-like atomic configurations is able to ensure that the fitted interatomic potentials provide a good representation of the screw dislocation Peierls barrier. The last two classes (EAM3 and EAM4) of potentials were derived similarly to the second class by selecting only the potentials with a reasonable shape of the Peierls barrier and the following additional properties: (i) for EAM3 we have fitted, in addition to the coefficients of the splines $\mathbf{A}$, also the cubic spline knots δ^{Φ} of the pair part (it is interesting to note that for this class, after fitting, the knots are grouped near the neighbour shell distances and can sometimes coincide with them, thus reducing the overall number of knots); (ii) for the fourth class (EAM4) we have decreased the weights w_E and w_{a_0} to 1 and 10, respectively. The appendix gives the numerical values of parameters for three of the potentials EAM2–4. Note that the EAM1 type is not included because of its poor representation of the variation of the screw dislocation core energy with respect to polarization (see section 4.5.1), although it is discussed in some of the following sections.

3. Point defects

To test the transferability of our potentials we have investigated the relative stability of small interstitial clusters: di-interstitial dumbbells I_2 and quadri-interstitial I_4 clusters, with both ⟨110⟩ and ⟨111⟩ dumbbell orientations; and the three-dimensional C15 clusters that were discovered recently [46]. The results are summarized in table 2. DFT GGA calculations were performed using the PWSCF

Table 2. Formation energies (in eV) of I_2 and I_4 clusters with different orientations computed using various empirical potentials and DFT calculations for a base supercell containing 128 atoms (either two or four atoms were added to create the defects). DFT GGA PBE calculations were performed with PWSCF and SIESTA codes using pseudopotentials with (sc) and without (without sc) the semi-core states in the electronic structure of a W atom, respectively. $E_f^{\langle 111\rangle}$ is the formation energy of the $\langle 111\rangle$ cluster. $\Delta E_f^{\langle 110\rangle,C15} = E_f^{\langle 110\rangle,C15} - E_f^{\langle 111\rangle}$, is the difference between the formation energy of the $\langle 110\rangle$ or C15 clusters and the formation energy of the corresponding $\langle 111\rangle$ cluster. A positive value of ΔE indicates that the $\langle 111\rangle$ cluster is more stable than the corresponding $\langle 110\rangle$ or C15 cluster.

	Interstitial clusters					
	I_2			I_4		
	$E_f^{\langle 111\rangle}$	$\Delta E_f^{\langle 110\rangle}$	ΔE_f^{C15}	$E_f^{\langle 111\rangle}$	$\Delta E_f^{\langle 110\rangle}$	ΔE_f^{C15}
FS	13.67	1.67	4.73	22.86	2.90	3.77
AT	15.39	1.38	4.43	25.50	3.20	3.22
DNMD	17.06	0.55	4.16	28.80	3.46	4.66
EAM2	18.15	1.15	2.18	35.73	2.70	−2.37
EAM3	18.19	1.51	5.12	32.53	1.88	2.92
EAM4	18.58	1.07	2.83	32.82	2.54	−1.62
DFT (sc)	19.12	0.67	5.16	29.50	1.90	1.87
DFT (without sc)	17.87	0.59	3.96	29.55	1.63	0.12

code [47]. The pseudopotentials were taken both with ($5s^2 5p^6 5d^4 6s^2$) and without ($5d^5 6s^1$) the semi-core states in the electronic structure of a W atom.

For all the interstitial clusters, the most stable types are those with the $\frac{1}{2}\langle 111\rangle$ orientation, corresponding to the shortest Burgers vector in the BCC lattice.

For the I_2 clusters, the C15 configuration is very unstable compared to the $\langle 111\rangle$ dumbbell, and spontaneous formation of such a structure is highly improbable. All the EAM potentials agree with DFT calculations in this respect. Nonetheless, we observe large scatter in the values of formation energies and their relative differences, depending on the pseudopotential used in the calculations, and on the contribution of semi-core electrons. This effect is also observed for I_4 clusters, where the difference in formation energies between $I_4^{\langle 111\rangle}$ and I_4^{C15} varies from 1.87 eV to 0.12 eV depending on the choice of the pseudopotential. The treatment of this effect is beyond the scope of this paper and requires further study. We also note that EAM2 and EAM4 potentials predict lower formation energy for the I_4^{C15} configuration than for $I_4^{\langle 111\rangle}$, at variance with the DFT calculations. The origin of this variance is beyond the scope of this paper and future versions of potentials should remove this undesirable property. However, we believe that this property of EAM2 and EAM4 potentials is not a severe drawback, and does not prevent the use of these potentials in large-scale simulations. Indeed, the phase space of C15 configurations is fairly difficult to reach if one starts from perfect BCC crystal structure. The only mechanism of formation of such configurations found so far is the growth of defects from smaller clusters formed in cascades [46]. The data given in table 2 show that the primary I_2^{C15} clusters are unstable compared to the $\langle 111\rangle$ clusters and hence cannot act as nucleation centres for the larger clusters during the initial stages of evolution of the cascades.

The formation energy of a mono-vacancy is in reasonable agreement with experiment and DFT calculations. The formation energies of small vacancy clusters computed using the new potentials are also in good overall agreement with experiment and DFT calculations. However, DFT calculations [48–51] indicate that a di-vacancy is weakly bound or even unbound (depending on the approximations involved in a DFT calculation) in the first-nearest-neighbour configuration (V_2^{1NN}) and is strongly repulsive in the second-nearest-neighbour configuration (V_2^{1NN}). All the EAM potentials developed so far, including those derived in this paper, are unable to reproduce this small vacancy cluster anomaly. This is illustrated in table 3, where both formation energies of small vacancy clusters and interaction energies of di-vacancies are given for the different potentials, and compared to DFT values from the literature.

We have checked the feasibility of producing an EAM potential with a repulsive V_2^{2NN} configuration by means of a special fitting procedure. This fit used a reduced database containing only the lattice parameters and cohesive energies of BCC/FCC structures together with the mono-vacancy and di-vacancy formation energies. The fitting procedure used, as the starting point, all the EAM parametrizations found after stage 3 of the original fitting (see section 2.2) and the methodology of that stage for the fitting itself. After adjustment, all the potentials predicted that vacancies are strongly bound in the first- and second-nearest-neighbour configurations of a di-vacancy—at odds with the DFT results [51]. This result reinforces the observation by Ventelon *et al* [51] that the LDOS (local density of states) of a di-vacancy exhibits changes between the first- and second-nearest-neighbour configurations, and these changes are most pronounced in the vicinity of the Fermi level. They show that in the electronic structure of V_2^{2NN} the number of states at the Fermi level increases compared to the V_2^{1NN} case. Those energy states just below the Fermi level become occupied, increasing the energy of V_2^{2NN} compared to the V_2^{1NN} configuration. Consequently, the second-nearest-neighbour configuration becomes energetically less favourable compared to the weakly bound or unbound V_2^{1NN} configuration. The EAM or second-moment tight-binding potentials presented here are not able to mimic this electronic effect and probably only the semi-empirical approaches based on high order

Table 3. Formation (E_f) and interaction (E_i) energies (in eV) of two-, three- and four-vacancy clusters computed using various empirical potentials and DFT calculations for a base supercell containing 128 atoms (from which atoms were removed to create the vacancy defects). The di-vacancy cluster V_2 is a configuration with the vacancies in the first-nearest-neighbour positions. The V_3 cluster is a triangle with two nearest-neighbour pairs and one second-nearest-neighbour pair. V_4 is a configuration obtained by adding one vacancy to V_3 in order to form a tetrahedron with four first-nearest-neighbour pairs and two second-nearest-neighbour pairs. The DFT calculations are labelled as [a] for Muzyk *et al* [50], who used the VASP code, and [b1] and [b2] for Ventelon *et al* [51], who used the PWSCF and SIESTA codes, and pseudopotentials with or without semi-core corrections, respectively. The DFT data of Becquart *et al* [49] are referred to as [c]. The interaction energy is the opposite of the binding energy, i.e. $E_i = 2 \times E_f^{V_1} - E_f^{V_2}$. Positive values of the interaction energy indicate repulsion between the vacancies, whereas negative values indicate attraction and imply vacancy clustering. $E_i^{V_2}$(1NN) and $E_i^{V_2}$(2NN) are the interaction energies for the first- and second-nearest-neighbour di-vacancy configurations, respectively.

	Cluster formation energies			V_2 Interaction energies	
Potential	$E_f^{V_2}$	$E_f^{V_3}$	$E_f^{V_4}$	$E_i^{V_2}$(1NN)	$E_i^{V_2}$(2NN)
FS/AT	6.83	9.57	11.77	−0.43	−0.40
DNMD	6.55	9.21	11.23	−0.57	−0.38
EAM2	6.48	0.94	11.02	−0.50	−0.39
EAM3	8.27	11.54	14.29	−0.45	−0.60
EAM4	7.11	9.90	12.07	−0.53	−0.46
DFT (sc)	7.13[a] 6.44[b1]	10.45[a]	13.40[a]	−0.01[a], 0.10[b1]	0.19[a], 0.46[b1]
DFT (without sc)	6.59[b2], 6.28[c]			0.15[b2], 0.06[c]	0.40[b2], 0.40[c]

moments, such as the orbital tight-binding formalism or BOP, will be able to take into account the above changes in the LDOS and in this way describe the di-vacancy non-binding effect.

4. Extended defects

4.1. Surfaces

Surface energy is defined as the excess energy per unit surface area for a particular termination of the crystal lattice. Surface energy plays an important part in surface physics where it influences faceting, crystal growth and other phenomena. Surface energies have been computed here using the slab technique [52, 53]. We treat only the relaxed and unreconstructed surfaces. The calculated surface energies, γ, for several surface orientations are given in figure 1. Empirical potentials underestimate the surface energies compared to DFT calculations, similarly to the BOP tight-binding approximation. It is interesting to note that the profiles of the curves for all the EAM potentials are approximately the same, with the exception of that for the DNMD potential. All the empirical approaches predict the (110) surface as the most stable termination, in agreement with the DFT and tight-binding treatments. Moreover, empirical potentials EAM4 and FS predict values that are of the same order of magnitude as those derived from BOP for the (110) and (211) surfaces. All the EAM potentials exhibit the tendency to overestimate the relative stability of γ_{111} and γ_{211} in relation to γ_{110} as compared to DFT calculations. The DNMD potential is an exception to this rule, and it exhibits agreement with DFT that is even better than that for tight-binding BOP calculations. We conclude that the new EAM potentials predict surface energies in good agreement with *ab initio* calculations, and the case of the DNMD potential shows the feasibility of developing potentials capable of predicting the correct relative stability of surfaces.

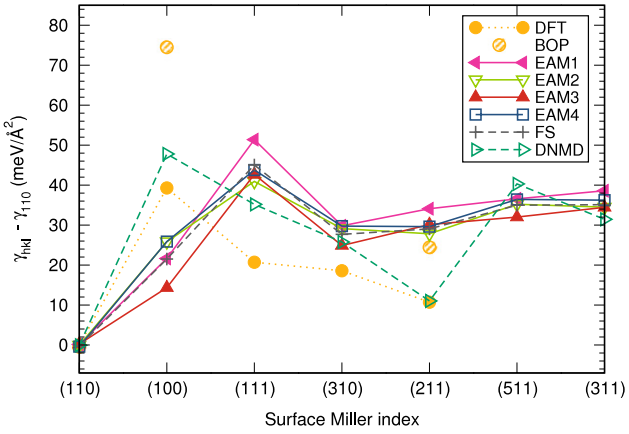

Figure 1. Surface energy γ per unit area at the surface for various tungsten surfaces, calculated using different models for interatomic interactions: Finnis and Sinclair [3] (FS), Derlet *et al* [33] (DNMD), the present EAM1–4 potentials, BOP and DFT. Energies for the Ackland and Thetford [7] (AT) potential are not shown because they are identical to those computed using the FS potential. The DFT and BOP data are taken from Vitos *et al* [53] and Mrovec *et al* [13], respectively. For each interatomic potential, the energy of the (110) surface γ_{110} is taken as a reference value. The values of γ_{110} are as follows, depending on the model for the interatomic forces used: $\gamma_{110}^{DFT} = 250$, $\gamma_{110}^{BOP} = 163$, $\gamma_{110}^{EAM1} = 195$, $\gamma_{110}^{EAM2} = 144$, $\gamma_{110}^{EAM3} = 193$, $\gamma_{110}^{EAM4} = 157$, $\gamma_{110}^{FS} = 161$, $\gamma_{110}^{DNMD} = 150$ (the values are in meV Å^{-2}). For all the interatomic potentials, particularly for EAM2 and EAM4, the (110) surface energy is significantly underestimated. The fact that EAM potentials underestimate the surface energy agrees with the results of Van Zwol *et al* [54] who found a similar systematic trend for BCC iron.

4.2. Gamma surfaces

A gamma surface is defined as the energy variation when the crystal is cut along a particular plane and then one of the resulting parts is displaced along a particular direction. This quantity is related to the energy landscape of dislocations

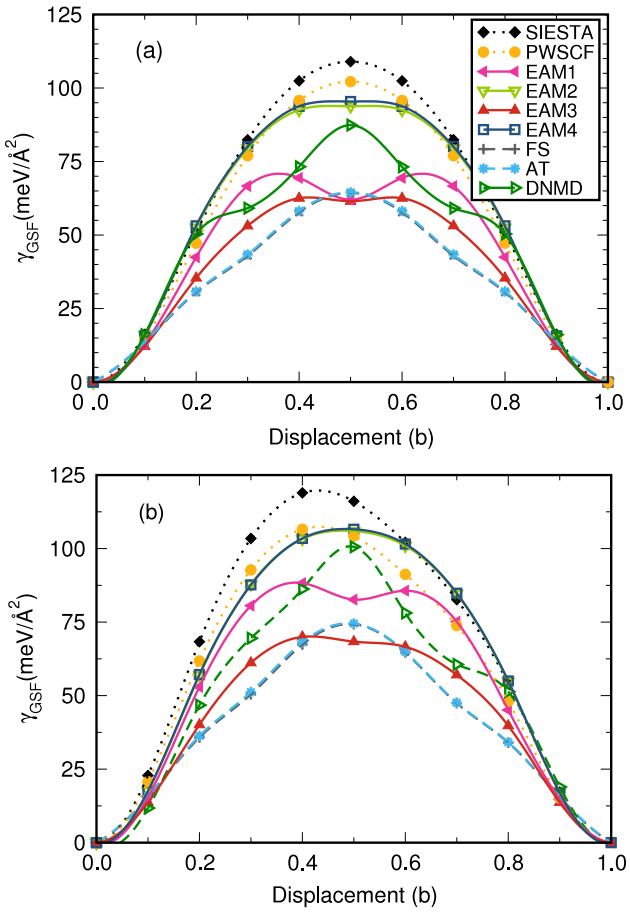

Figure 2. Cross-sections, along the ⟨111⟩ direction, of the generalized stacking fault (GSF) gamma surfaces in the (a) {110} and (b) {211} planes derived from DFT calculations performed using SIESTA and PWSCF GGA with pseudopotentials without the semi-core states, and the empirical potentials. The x-axis displacement is given as a fraction of the $\mathbf{b} = \frac{1}{2}[111]$ Burgers vector.

[40, 41] and provides data out of equilibrium, preserving the crystal state. In this section we compute the gamma surface in a BCC crystal which is cut into two parts along either the {110} or the {211} planes, and the parts are then displaced along the ⟨111⟩ direction, as described in [42]. The ⟨111⟩ cross-sections of the {110} and {211} gamma surfaces are shown in figure 2. The four empirical potentials predict gamma surfaces of fairly similar shape, in agreement with SIESTA and PWSCF DFT calculations, as well as with other DFT calculations [55, 56].

4.3. The Bain transformation

Both BCC and FCC lattices represent special cases of the centred tetragonal Bravais lattice. The BCC structure can be transformed into the FCC structure along the so-called Bain, or tetragonal, pathway by stretching the initial BCC crystal at a constant volume along the [001] axis. Using the value of $r = c/a$ as the reaction coordinate (here a is the side of the square base and c is the height of the tetragonal cell), the high symmetry BCC and FCC structures correspond to $r = 1$ and

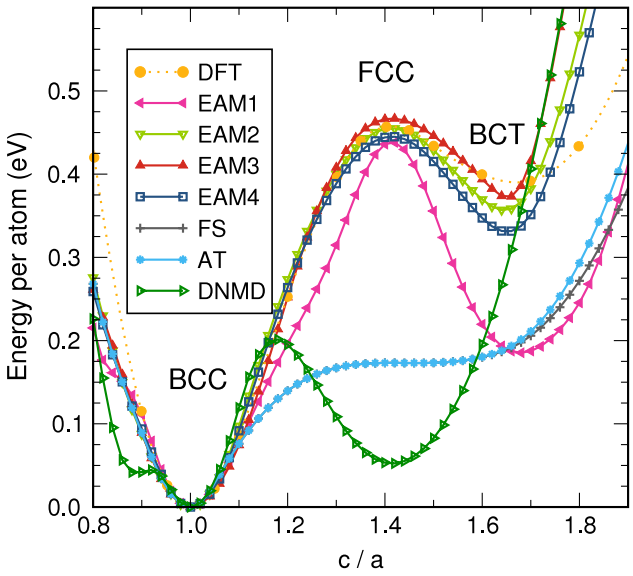

Figure 3. Variation of energy per atom calculated for the tetragonal Bain deformation pathway using the EAM potentials and DFT. The DFT PBE GGA data are taken from [13]. The reference energy is the cohesive energy of the BCC structure.

$r = \sqrt{2}$, respectively. For larger deformations we find another special structure, known as body-centred tetragonal (BCT), which corresponds to a local energy minimum at $r \approx 1.7$. The value of ideal tensile strength in the ⟨100⟩ direction in the BCC lattice results from the competition between instabilities associated with the BCT and FCC saddle-point structures [57].

Figure 3 shows how energy per atom varies along the Bain reaction pathway. EAM2–4 follow closely the DFT Bain path, showing that the ideal tensile stress and strain are in good agreement with the *ab initio* values. This is a significant advance, as the EAM potentials developed earlier [3, 7, 33] (also shown in the figure) predict that the FCC structure is not a local energy *maximum* but a local *minimum* or a saddle point, at odds with *ab initio* calculations.

4.4. The atomic string model

Gilbert and Dudarev [26] recently applied a multi-string Frenkel–Kontorova (MSFK) model to investigate how to guarantee that an interatomic potential predicts the same core structure for a $\frac{1}{2}\langle 111\rangle$ screw dislocation as was derived from 0 K DFT calculations. In particular, they found that it is the shape of the ΔE curve, calculated, for a given potential, by rigidly displacing a [111] atomic string (row) through an otherwise perfect BCC lattice, that determines the favoured equilibrium core structure of the $\frac{1}{2}\langle 111\rangle$ screw dislocation. It is also expected that the energy versus atomic string displacement curves associated with two adjacent (first-nearest-neighbour) strings moving rigidly together, or in opposition (shear), will help analyse the energetics (and dynamics) associated with the migration of screw dislocations via the formation of kink-pairs. Here we investigate how well

our new potentials reproduce the shape and magnitude of these atomic string displacement curves calculated from DFT.

Figure 4 shows, in three separate panels, the variation in energy associated with the displacement of a single [111] string, a pair of first-nearest-neighbour (1NN) strings in the same direction, and from shearing a 1NN pair. As was noted in [26], the 1NN string–string interaction represents the leading term in the Hamiltonian of the MSFK model, and indeed here we find that the ΔE curves for the displacement of the 2NN or 3NN strings (shear or otherwise) are very close to the single-string curve with the appropriate multiplication factor. In each graph, results are shown for the EAM2–4 potentials, along with the equivalent calculations from DFT, performed using GGA for a rectangular 48-atom cell defined in the $x \parallel [1\bar{1}0]$, $y \parallel [11\bar{2}]$, and $z \parallel [111]$ coordinate system. For comparison, we also show the curves computed for the AT and the DNMD potentials for W. Both of these latter potentials are known to predict the incorrect degenerate core structure for the $\frac{1}{2}\langle 111\rangle$ screw dislocation.

From figure 4 it is clear that the EAM3 potential provides the best match to both the shape and magnitude of the DFT curves, although all of the potentials developed in the present work represent a significant improvement on the previous attempts to find a semi-empirical interatomic potential for tungsten. Specifically, the curves computed for EAM2–4 all show good agreement to both the shape and magnitude of the DFT results associated with rigid displacements of both a single [111] string, and two 1NN strings in the same direction. Thus, even though the fitting procedure used in this work did not explicitly include these displacement curves (as was suggested in [26, 58]), the potentials all correctly predict the non-degenerate compact screw dislocation core at 0 K. The fact that the DFT-computed energy–displacement curves produced by shearing two 1NN strings agree well with the curves computed using the new EAM potentials suggests that they may also correctly represent some of the more subtle aspects of the behaviour of screw dislocations, for example the thermally activated mobility of dislocations under applied stress.

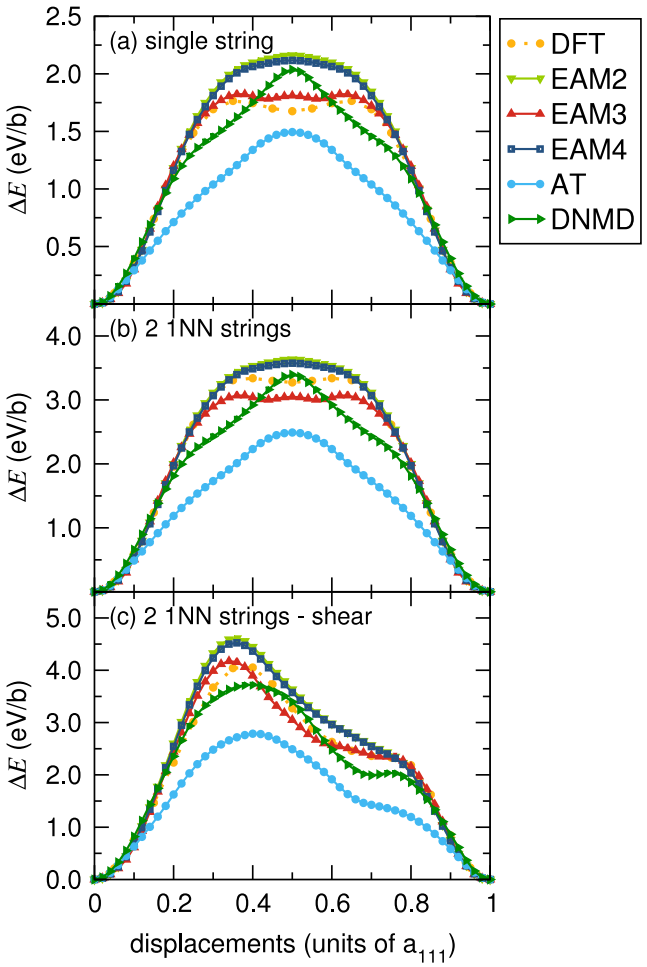

Figure 4. Energy variation associated with the rigid displacement of different strings of atoms: (a) a single [111] string displaced through the lattice; (b) two first-nearest-neighbour (two 1NN) strings displaced in the same direction; (c) two 1NN strings displaced in opposite directions (shear). The string displacement curves calculated using the empirical potentials are compared with those derived from DFT.

4.5. Screw dislocation

For all the newly developed empirical potentials we have computed the basic properties of the $\langle 111\rangle$ screw dislocations: the core structure of the dislocations, the polarization of the dislocation core, the Peierls barrier, the Peierls stress, the glide plane, and the formation energy of the double kinks.

4.5.1. Polarization. The approach to the screw dislocation calculations that we adopted in this work involves a quadrupolar periodic array of dislocation dipoles [27, 28]. An investigation of the effect of the cell size shows that energy convergence was achieved for cell sizes of 135 atoms b^{-1} within DFT. The empirical potentials calculation were performed using cell sizes of 1215 atoms b^{-1}.

As was noted above, the EAM1–4 potentials yield a non-degenerate core structure, as predicted from DFT calculations performed using the SIESTA and PWSCF codes [28], in agreement with other recent DFT calculations [56, 59]. To our knowledge the potentials presented in this paper are the first many-body EAM-type potentials to predict the correct non-degenerate core structure for the screw dislocation in W [13, 28, 30, 60–62].

The relative stability of the degenerate and non-degenerate core configurations was investigated by calculating the dependence of the dislocation core energy on its polarization. By analysing the polarization of the core one can distinguish a non-degenerate core structure from a degenerate core structure. The polarization parameter is defined in terms of the displacement of atomic strings, described above, along the [111] direction. Specifically, to characterize a $\frac{1}{2}\langle 111\rangle$ dislocation, we use the displacement of the three central atomic strings relative to the next three atomic strings, as explained in [42]. In these calculations, constrained minimization is performed in such a way that the value of the polarization parameter is kept fixed, while all the other degrees of freedom are relaxed. The results

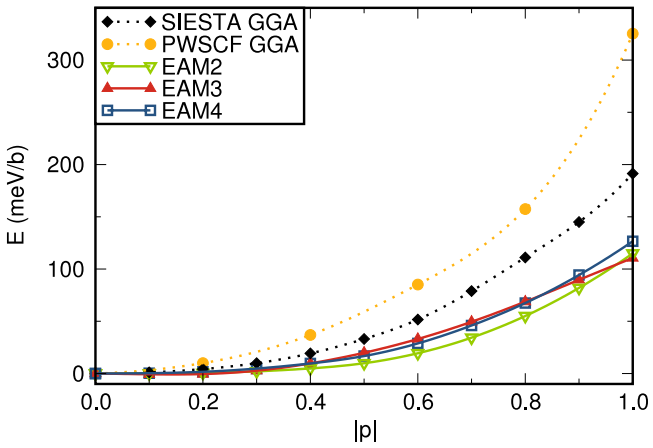

Figure 5. Variation of the dislocation core energy as a function of its polarization calculated using DFT and empirical potentials.

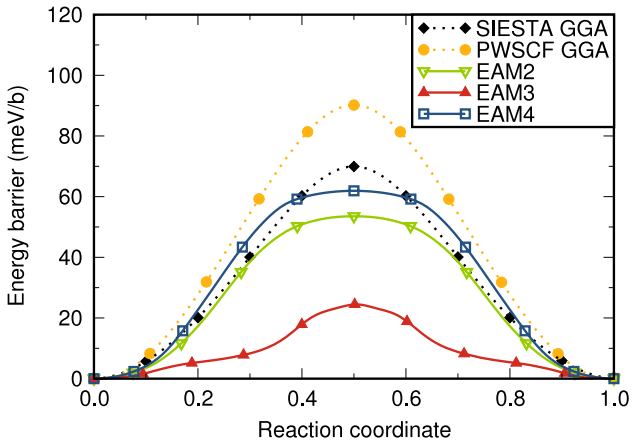

Figure 6. Peierls energy barrier calculated for tungsten using DFT and empirical potentials. The PWSCF and empirical potentials barriers were computed using the NEB method while the SIESTA barrier is computed using the reaction coordinate method.

obtained for the empirical potentials and from DFT are shown in figure 5. In the case of potentials EAM2–4, these calculations confirm that a stable dislocation core is entirely unpolarized. Calculations show no evidence of the occurrence of any metastable polarized core, in agreement with our DFT calculations and other recent DFT results [59]. Using a criterion involving the variation of the core energy with respect to its polarization, the EAM1 potential displays very different behaviour as compared to DFT data. Consequently, this potential was eliminated from other validation tests related to screw dislocations discussed in this paper, and its parameters are not given in the appendix.

4.5.2. The Peierls barrier for a screw dislocation. The Peierls barrier for a $\frac{1}{2}\langle 111\rangle$ screw dislocation was calculated by displacing simultaneously in the {110} plane the two dislocations forming the dipole in such a way that their separation distance remained constant. A nudged elastic band (NEB) [63] calculation was then performed and the elastic contribution due to the different elastic strains associated with the initial and final states was then subtracted. For EAM2–4 the resulting Peierls barrier exhibits a single-humped profile, in agreement with DFT results. The EAM4 potential predicts a barrier height that agrees best with the DFT values.

4.5.3. The Peierls stress and kink energies. To compute the Peierls stress, shear stress was applied to the dislocation cell until the dislocation began to glide. Simulation cells of two types were used: (i) with free surfaces parallel to the {110} plane as in Rodney *et al* [64] and (ii) using a quadrupolar arrangement of dislocation dipoles with tri-periodic boundary conditions. The Peierls stress values obtained with both methods, as well as the glide plane, are given in table 4. Only EAM3 potential predicts a {110} glide plane, in agreement with experiment [65, 66] and DFT calculations [59]. The Peierls stress obtained with this potential is close to 1.1 GPa. EAM2 and EAM4 potentials, even though they give more accurate predictions for the Peierls barrier (figure 6), show zigzag movement on {110} planes resulting in an average

Table 4. Peierls energy (in meV b^{-1}, ±5 meV b^{-1}), Peierls stress (in GPa, ±0.1 GPa) and the glide plane calculated for tungsten using empirical potentials. For comparison, experimental results from [67] are also reported, as well as the DFT Peierls energies computed using SIESTA and PWSCF, extracted from figure 6.

	Peierls energy	Peierls stress	Glide plane
EAM2	53	1.75	{211}
EAM3	24	1.14	{110}
EAM4	62	2.03	{211}
Experiment		0.98	{110}
SIESTA	70	—	—
PWSCF	90	—	—

Table 5. Kink formation energies (in eV) calculated for the $\frac{1}{2}\langle 111\rangle$ screw dislocation in tungsten using the three EAM potentials developed in this work. For comparison, the experimental value of 2.1 eV for the kink-pair formation energy is taken from [67, 69]. The SIESTA and PWSCF values are derived by interpolating the scaling law based on the Frenkel–Kontorova model (see figure 7) to the corresponding values of the Peierls energy barrier.

	Left kink	Right kink	Kink-pair
EAM2	0.61	0.83	1.44
EAM3	0.27	0.48	0.75
EAM4	0.71	0.92	1.63
Experiment	—	—	2.10
SIESTA	—	—	1.77
PWSCF	—	—	2.10

{211} glide plane. The EAM3 potential appears to be the only potential for tungsten reproducing both the single-hump Peierls barrier and the {110} glide plane.

The kink energies were calculated using a slice of 100 b for the case of a single-kink calculation, and 200 b in the case of a double-kink or kink-pair calculation. Details of the methodology used for kink calculations can be found in [68]. The calculated values of the kink formation energies are given in table 5. Of the three empirical potentials, two predict a kink-pair energy in relatively good agreement with

experimental observations, where the data from the work by Brunner [67] (low stress regime and $T = 600$ K) and Giannattasio *et al* [69] show that the formation energy of a kink-pair on a $\frac{1}{2}\langle 111\rangle$ screw dislocation is close to 2.1 eV.

To gain deeper understanding of what influences the formation energy of a kink-pair, we plotted the calculated values of the kink-pair formation energies against the square root of the Peierls energy (figure 7). Linear scaling of the kink-pair energy as a function of the square root of the Peierls energy is expected from the discrete Frenkel–Kontorova model (see equations (9) and (11) of [70]) or from the continuous limit of the Frenkel–Kontorova model: the string under tension model of Eshelby (equations (2.4) and (2.5) of [71]). Figure 7 shows that the kink-pair formation energies computed using EAM2–4 potentials scale almost exactly linearly as a function of the square root of the Peierls energy. This suggests that these three potentials are characterized by almost identical values of the effective dislocation line tension. The fact that all the three potentials agree well with the DFT atomic strings energy–displacement curves shown in figure 4 confirms that this is likely to be the case, an assertion also supported by the high accuracy of linear scaling seen in figure 7. It should be noted that the Peierls potential plays an important role as a variable against which the scaling is observed. Potentials with a double-hump shape of the Peierls potential will not follow the same linear regime. From this perspective it is crucial to have potentials in qualitative agreement with the DFT calculations. We assume that the effective line tension computed from the EAM2–4 also applies to *ab initio* computations where the kink-pair computations cannot be carried out directly because the required simulation cell size is beyond the capability of electronic structure calculations. According to this assumption, the linear scaling should also apply to *ab initio* data and we obtain values for the kink-pair formation energies corresponding to the Peierls barriers calculated using SIESTA and PWSCF codes of 1.78 eV and 2.1 eV, respectively. The latter value appears to agree well with experimental data [67, 69]. This prediction of the experimental value of the kink-pair formation energy shows the generality of the line string model in the low stress regime with respect to the interatomic interaction [70, 72].

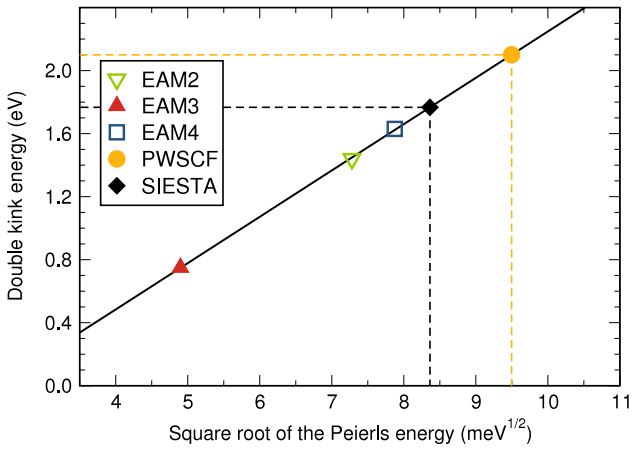

Figure 7. Double-kink formation energy on the $\frac{1}{2}\langle 111\rangle$ screw dislocation plotted as a function of the square root of the Peierls barrier energy. A linear relation between the two quantities is expected from the Frenkel–Kontorova model, assuming a constant value of the effective line tension [70]. The dashed lines from the two DFT data sets (PWSCF and SIESTA) indicate that the kink-pair formation energies are estimated using values of the Peierls energy given in table 4 and the linear fit obtained for the EAM potentials (solid line).

5. Conclusions

We have developed and tested empirical interatomic potentials for simulating radiation defects and dislocations in tungsten. The potentials use the embedded atom method formalism and have been fitted to a mixed database, which contains experimentally measured values of various physical parameters of crystalline tungsten, *ab initio* information on formation energies of defect clusters, and *ab initio* atomic forces derived from random liquid configurations. The potentials have been extensively tested against *ab initio* and experimental values, including the *ab initio* data (for example the atomic string energy–displacement curves) that were not included in the fitting database.

The potentials show reasonable performance in the treatment of radiation defects and are the first EAM potentials for tungsten that are in qualitative agreement with DFT calculations on screw dislocations. However, some of the properties of the potentials could still be improved, including the SIA formation energies and the surface energies. We also note that none of the potentials are able to reproduce repulsive interaction between vacancies in the second-nearest-neighbour configuration. Nevertheless, the potentials provide a useful start for future developments and analysis.

More importantly, these potentials provide acceptable EAM parametrizations adapted to the physics of screw dislocations in tungsten, a problem that has so far proved difficult to resolve using many of the potentials available in the literature. This will enable, for the first time, large-scale time–space simulations of dislocations in tungsten. For example, Cereceda *et al* [73] recently investigated the finite temperature properties of screw dislocations in tungsten using molecular dynamics (note that the EAM3 potential of [73] is the same as the EAM2 potential described here). The EAM4 potential can be preferentially used to study properties of screw dislocations because the magnitude of the Peierls potential and the kink-pair energy are the closest to the experimental and DFT values. However, the EAM3 potential is also useful since, on average, it represents general properties well, and also yields a qualitatively good Peierls barrier and the correct (110) glide plane for the screw dislocation (which is not the case for the EAM4 potential).

More importantly, all three parametrizations proposed here should enable future comparative studies aimed at the testing and improvement of various theoretical models. This paper gives possibly the first example of this kind:

namely a trend predicted for the Peierls barrier of the $\frac{1}{2}\langle 111\rangle$ screw dislocation that is in qualitative agreement with *ab initio* calculations, enabling the comparison of predicted kink-pair formation energies with experimental data. We find that the predicted value of the kink-pair formation energy depends sensitively on the Peierls energy for the $\frac{1}{2}\langle 111\rangle$ screw dislocation, in agreement with scaling derived from the Frenkel–Kontorova model. This enables prediction of the kink-pair formation energy from *ab initio* data on straight screw dislocations, in good agreement with experiment.

Other than the screw dislocation related topics, these potentials are well suited to the study of other areas, such as liquid properties, the high temperature and/or pressure properties at melting temperature, the pressure–volume–temperature equation of state, and the temperature variation of elastic properties. All these quantities should also be target properties of future potential development studies.

Acknowledgments

This work was performed using HPC resources from GENCI-[CCRT/CINES] (Grants x2013096821 and x2013096973). Part of this work was performed using HPC resources from 5th PRACE access on MareNostrum III at BSC under the DIMAIM project. This work was also partly funded by the RCUK Energy Programme under grant EP/I501045 and the European Communities under Contracts of Association between EURATOM and CEA, and EURATOM and CCFE, under programme grant EP/H018921/1 'Materials for Fission and Fusion Power', and also by the EURATOM staff mobility programme. The views and opinions expressed herein do not necessarily reflect those of the European Commission. This work was carried out within the framework of the European Fusion Development Agreement. We would like to thank Dr D R Mason for useful discussions.

Appendix

Tables A.1, A.2, and A.3 give the numerical values of parameters for potentials EAM2, EAM3 and EAM4, respectively.

With the present set of parameters the density $\rho(x)$ has, in the zero-distance limit, a negative value. This unphysical behaviour can yield numerical instabilities. In order to overcome this inconvenience, it is recommended to use following modified version of the density $\rho_n(x)$:

$$\rho_n(x) = \begin{cases} \rho(r_c) & \text{for } x \le r_c, \\ \rho(x) & \text{for } x > r_c. \end{cases} \tag{6}$$

$\rho(x)$ is the density function defined by equation (3) and $r_c = 2.002\,970\,124\,727$ Å.

Table A.1. Parameters of the empirical potential EAM2 for tungsten. The notation corresponds to equations (1)–(4). Cubic spline knots are expressed in Å and coefficients of cubic polynomials for Φ and F in eV.

	EAM2	
a_1^Φ (δ_1^Φ)	$0.960\,851\,701\,343\,041\times10^{2}$	(2.564 897 500 000 000)
a_2^Φ (δ_2^Φ)	$-0.184\,410\,923\,895\,214\times10^{3}$	(2.629 795 000 000 000)
a_3^Φ (δ_3^Φ)	$0.935\,784\,079\,613\,550\times10^{2}$	(2.694 692 500 000 000)
a_4^Φ (δ_4^Φ)	$-0.798\,358\,265\,041\,677\times10^{1}$	(2.866 317 500 000 000)
a_5^Φ (δ_5^Φ)	$0.747\,034\,092\,936\,229\times10^{1}$	(2.973 045 000 000 000)
a_6^Φ (δ_6^Φ)	$-0.152\,756\,043\,708\,453\times10^{1}$	(3.079 772 500 000 000)
a_7^Φ (δ_7^Φ)	$0.125\,205\,932\,634\,393\times10^{1}$	(3.516 472 500 000 000)
a_8^Φ (δ_8^Φ)	$0.163\,082\,162\,159\,425\times10^{1}$	(3.846 445 000 000 000)
a_9^Φ (δ_9^Φ)	$-0.141\,854\,775\,352\,260\times10^{1}$	(4.176 417 500 000 000)
a_{10}^Φ (δ_{10}^Φ)	$-0.819\,936\,046\,256\,149\times10^{0}$	(4.700 845 000 000 000)
a_{11}^Φ (δ_{11}^Φ)	$0.198\,013\,514\,305\,908\times10^{1}$	(4.895 300 000 000 000)
a_{12}^Φ (δ_{12}^Φ)	$-0.696\,430\,179\,520\,267\times10^{0}$	(5.089 755 000 000 000)
a_{13}^Φ (δ_{13}^Φ)	$0.304\,546\,909\,722\,160\times10^{-1}$	(5.342 952 500 000 000)
a_{14}^Φ (δ_{14}^Φ)	$-0.163\,131\,143\,161\,660\times10^{1}$	(5.401 695 000 000 000)
a_{15}^Φ (δ_{15}^Φ)	$0.138\,409\,896\,486\,177\times10^{1}$	(5.460 437 500 000 000)
a_1^ρ (δ_1^ρ)	$-0.420\,429\,107\,805\,055\times10^{1}$	(2.500 000 000 000 000)
a_2^ρ (δ_2^ρ)	$0.518\,217\,702\,261\,442\times10^{0}$	(3.100 000 000 000 000)
a_3^ρ (δ_3^ρ)	$0.562\,720\,834\,534\,370\times10^{-1}$	(3.500 000 000 000 000)
a_4^ρ (δ_4^ρ)	$0.344\,164\,178\,842\,340\times10^{-1}$	(4.900 000 000 000 000)
a_1^F	$-5.946\,454\,472\,402\,710$	
a_2^F	$-0.049\,477\,376\,935\,239$	

Table A.2. Parameters of the empirical potential EAM3 for tungsten. The notation corresponds to equations (1)–(4). Cubic spline knots are expressed in Å and coefficients of cubic polynomials for Φ and F in eV.

	EAM3	
a_1^{Φ} (δ_1^{Φ})	0.335 180 090 207 171 $\times 10^{3}$	(2.610 000 000 000 000)
a_2^{Φ} (δ_2^{Φ})	−0.630 187 843 239 795 $\times 10^{3}$	(2.680 000 000 000 000)
a_3^{Φ} (δ_3^{Φ})	0.351 436 490 059 390 $\times 10^{3}$	(2.718 160 253 915 930)
a_4^{Φ} (δ_4^{Φ})	−0.187 104 554 936 536 $\times 10^{-1}$	(2.758 522 910 939 240)
a_5^{Φ} (δ_5^{Φ})	0.599 698 179 163 370 $\times 10^{-1}$	(2.892 427 681 390 960)
a_6^{Φ} (δ_6^{Φ})	−0.210 635 074 070 024 $\times 10^{-1}$	(3.401 517 108 884 100)
a_7^{Φ} (δ_7^{Φ})	0.258 575 483 268 791 $\times 10^{-1}$	(3.675 283 167 162 630)
a_8^{Φ} (δ_8^{Φ})	0.389 896 994 857 220 $\times 10^{-1}$	(4.248 392 613 157 640)
a_9^{Φ} (δ_9^{Φ})	−0.139 737 073 858 817 $\times 10^{-1}$	(4.631 029 170 086 540)
a_{10}^{Φ} (δ_{10}^{Φ})	0.184 785 876 328 131 $\times 10^{-1}$	(4.822 645 095 086 770)
a_{11}^{Φ} (δ_{11}^{Φ})	−0.505 971 175 928 021 $\times 10^{0}$	(5.021 214 835 934 140)
a_{12}^{Φ} (δ_{12}^{Φ})	−0.890 738 292 956 047D $\times 10^{1}$	(5.282 885 848 627 100)
a_{13}^{Φ} (δ_{13}^{Φ})	0.495 992 901 621 487 $\times 10^{-1}$	(5.283 029 247 305 360)
a_{14}^{Φ} (δ_{14}^{Φ})	0.377 639 491 131 043 $\times 10^{-1}$	(5.290 925 630 219 230)
a_1^{ρ} (δ_1^{ρ})	−0.420 429 107 805 055 $\times 10^{-1}$	(2.500 000 000 000 000)
a_2^{ρ} (δ_2^{ρ})	0.518 217 702 261 442 $\times 10^{0}$	(3.100 000 000 000 000)
a_3^{ρ} (δ_3^{ρ})	0.562 720 834 534 370 $\times 10^{-1}$	(3.500 000 000 000 000)
a_4^{ρ} (δ_4^{ρ})	0.344 164 178 842 340 $\times 10^{-1}$	(4.900 000 000 000 000)
a_1^{F}	−5.073 237 905 708 500	
a_2^{F}	−0.039 263 610 952 181	

Table A.3. Parameters of the empirical potential EAM4 for tungsten. The notation corresponds to equations (1)–(4). Cubic spline knots are expressed in Å and coefficients of cubic polynomials for Φ and F in eV.

	EAM4	
a_1^{Φ} (δ_1^{Φ})	0.954 071 477 542 914 $\times 10^{2}$	(2.564 897 500 000 000)
a_2^{Φ} (δ_2^{Φ})	−0.181 161 004 448 916 $\times 10^{3}$	(2.629 795 000 000 000)
a_3^{Φ} (δ_3^{Φ})	0.930 215 233 132 627 $\times 10^{2}$	(2.694 692 500 000 000)
a_4^{Φ} (δ_4^{Φ})	−0.108 428 907 515 182 $\times 10^{2}$	(2.866 317 500 000 000)
a_5^{Φ} (δ_5^{Φ})	0.112 027 468 539 573 $\times 10^{2}$	(2.973 045 000 000 000)
a_6^{Φ} (δ_6^{Φ})	−0.312 459 176 640 227 $\times 10^{1}$	(3.079 772 500 000 000)
a_7^{Φ} (δ_7^{Φ})	0.123 028 140 617 302 $\times 10^{1}$	(3.516 472 500 000 000)
a_8^{Φ} (δ_8^{Φ})	0.154 767 467 307 454 $\times 10^{1}$	(3.846 445 000 000 000)
a_9^{Φ} (δ_9^{Φ})	−0.128 861 387 780 439 $\times 10^{1}$	(4.176 417 500 000 000)
a_{10}^{Φ} (δ_{10}^{Φ})	−0.843 327 493 551 467 $\times 10^{0}$	(4.700 845 000 000 000)
a_{11}^{Φ} (δ_{11}^{Φ})	0.214 009 882 965 042 $\times 10^{1}$	(4.895 300 000 000 000)
a_{12}^{Φ} (δ_{12}^{Φ})	−0.102 898 314 532 388 $\times 10^{1}$	(5.089 755 000 000 000)
a_{13}^{Φ} (δ_{13}^{Φ})	0.138 163 259 601 912 $\times 10^{1}$	(5.342 952 500 000 000)
a_{14}^{Φ} (δ_{14}^{Φ})	−0.360 872 433 001 551 $\times 10^{1}$	(5.401 695 000 000 000)
a_{15}^{Φ} (δ_{15}^{Φ})	0.217 655 968 740 690 $\times 10^{1}$	(5.460 437 500 000 000)
a_1^{ρ} (δ_1^{ρ})	−0.420 429 107 805 055 $\times 10^{1}$	(2.500 000 000 000 000)
a_2^{ρ} (δ_2^{ρ})	0.518 217 702 261 442 $\times 10^{0}$	(3.100 000 000 000 000)
a_3^{ρ} (δ_3^{ρ})	0.562 720 834 534 370 $\times 10^{-1}$	(3.500 000 000 000 000)
a_4^{ρ} (δ_4^{ρ})	0.344 164 178 842 340 $\times 10^{-1}$	(4.900 000 000 000 000)
a_1^{F}	−5.553 986 589 859 130	
a_2^{F}	−0.045 691 157 657 292	

References

[1] Daw M S and Baskes M J 1987 Embedded-atom method: derivation and application to impurities, surfaces, and other defects in metals *Phys. Rev.* B **29** 6443

[2] Sutton A P and Chen J 1984 Long-range Finnis–Sinclair potentials *Phil. Mag. Lett.* **61** 139

[3] Finnis M W and Sinclair J E 1984 A simple empirical n-body potential for transition metals *Phil. Mag.* A **50** 45

[4] Daw M S, Foiles S M and Baskes M I 1993 The embedded-atom method: review of theory and applications *Mater. Sci. Rep.* **9** 251–310

[5] Pettifor D G 1995 *Bonding and Structure of Molecules and Solids* (Oxford: Clarendon)

[6] Finnis M W 2003 *Interatomic Forces in Condensed Matter* (Oxford: Oxford University Press)

[7] Ackland G J and Thetford R 1987 An improved n-body semi-empirical model for body-centred cubic transition metals *Phil. Mag.* A **56** 15

[8] Baskes M I 1992 Modified embedded-atom potentials for cubic materials and impurities *Phys. Rev.* B **46** 2727

[9] Desjonquéres M C and Spanjaard D 1993 *Concepts in Surface Physics* (New York: Springer)

[10] Pettifor D G 1989 New many-body potential for the bond order *Phys. Rev. Lett.* **63** 2480

[11] Horsfield A P, Bratkovsky A M, Fearn M, Pettifor D G and Aoki M 1996 Bond-order potentials: theory and implementation *Phys. Rev.* B **53** 12694

[12] Mrovec M, Nguyen-Manh D, Pettifor D G and Vitek V 2004 Bond-order potential for molybdenum: application to dislocation behaviour *Phys. Rev.* B **69** 094115

[13] Mrovec M, Gröger R, Bailey A G, Nguyen-Manh D, Elsässer C and Vitek V 2007 Bond-order potential for simulations of extended defects in tungsten *Phys. Rev.* B **75** 104119

[14] Ahlgren T, Heinola K, Juslin N and Kuronen A 2010 Bond-order potential for point and extended defect simulations in tungsten *J. Appl. Phys.* **107** 033516

[15] Mrovec M, Nguyen-Manh D, Elsässer C and Gumbsch P 2011 Magnetic bond-order potential for iron *Phys. Rev. Lett.* **106** 246402

[16] Ercolessi F and Adams J B 1994 Interatomic potentials from first-principles calculations: the force-matching method *Europhys. Lett.* **26** 583

[17] Ackland G J, Bacon D J, Calder A F and Harry T 1997 Computer simulation of point defect properties in dilute Fe–Cu alloy using a many-body interatomic potential *Phil. Mag.* A **75** 713

[18] Mishin Y, Mehl M J, Papaconstantopoulos D A, Voter A F and Kress J D 2001 Structural stability and lattice defects in cooper: *ab initio*, tight binding and EAM calculations *Phys. Rev.* B **63** 224106

[19] Mendelev M I, Srolovitz D J, Ackland G J, Sun D Y and Asta M 2003 Development of new interatomic potentials appropriate for crystalline and liquid iron *Phil. Mag.* **83** 3977

[20] Ackland G J, Mendelev M I, Srolovitz D J, Han S and Barashev A V 2004 Development of an interatomic potential for phosphorus impurities in α-iron *J. Phys.: Condens. Matter* **16** S2629

[21] Gordon P A, Neeraj T and Mendelev M I 2011 Screw dislocation mobility in BCC metals: a refined potential description for α-Fe *Phil. Mag.* **91** 3931

[22] Malerba L *et al* 2010 Comparison of empirical interatomic potentials for iron applied to radiation damage studies *J. Nucl. Mater.* **406** 19

[23] Dudarev S L and Derlet P M 2005 A magnetic interatomic potential for molecular dynamics simulations *J. Phys.: Condens. Matter* **17** 7097

[24] Chiesa S, Derlet P M and Dudarev S L 2009 Free energy of a $\langle 110 \rangle$ dumbbell interstitial defect in BCC Fe: harmonic and anharmonic contributions *Phys. Rev.* B **79** 214109

[25] Chiesa S, Derlet P M, Dudarev S L and Van Swygenhoven H 2011 Optimization of the magnetic potential for α-Fe *J. Phys.: Condens. Matter* **23** 206001

[26] Gilbert M R and Dudarev S L 2010 *Ab initio* multi-string Frenkel–Kontorova model for a $b = a/2[111]$ screw dislocation in BCC iron *Phil. Mag.* **90** 1035

[27] Ventelon L and Willaime F 2007 Core structure and peierls potential of screw dislocations in α-Fe from first principles: cluster versus dipole approaches *J. Comput.-Aid. Mater. Des.* **14** 85

[28] Ventelon L, Clouet E, Willaime F and Rodney D 2013 *Ab initio* investigation of the Peierls potential of screw dislocations in BCC Fe and W *Acta Mater.* **61** 3973

[29] Proville L, Rodney D and Marinica M-C 2012 Quantum effect on thermally activated glide of dislocations *Nature Mater.* **11** 845

[30] Duesbery M S and Vitek V 1998 Plastic anisotropy in b.c.c. transition metals *Acta Mater.* **46** 1481

[31] Juslin N and Wirth B D 2013 Interatomic potentials for simulation of He bubble formation in W *J. Nucl. Mater.* **432** 61

[32] Wang Y R and Boercker D B 1995 Effective interatomic potential for body-centered-cubic metals *J. Appl. Phys.* **78** 122

[33] Derlet P M, Nguyen-Manh D and Dudarev S L 2007 Multiscale modeling of crowdion and vacancy defects in body-centered-cubic transition metals *Phys. Rev.* B **76** 5

[34] Dudarev S L 2008 The non-Arrhenius migration of interstitial defects in BCC transition metals *C. R. Physique* **9** 409

[35] Errico R M 1997 What is an adjoint model? *Bull. Am. Meteorol. Soc.* **78** 2577

[36] Giering R and Kaminski T 1998 Recipes for adjoint code construction *ACM Trans. Math. Softw.* **24** 437

[37] Documentation du code ASSIMPOT: bases théoriques et utilisation, note interne EDF, HI-23/05/003/A

[38] Becquart C S, Raulot J M, Bencteux G, Domain C, Perez M, Garruchet S and Nguyen H 2007 Atomistic modeling of an Fe system with a small concentration of C *Comput. Mater. Sci.* **40** 119

[39] Soler J M, Artacho E, Gale J D, García A, Junquera J, Ordejón P and Sánchez-Portal D 2002 The SIESTA method for *ab initio* order-n materials simulation *J. Phys.: Condens. Matter* **14** 2745

[40] Peierls R E 1940 The size of a dislocation *Proc. Phys. Soc.* **52** 34

[41] Nabarro F R N 1947 Dislocations in a simple cubic lattice *Proc. Phys. Soc.* **59** 256

[42] Ventelon L and Willaime F 2010 Generalized stacking-faults and screw-dislocation core-structure in BCC iron: a comparison between *ab initio* calculations and empirical potentials *Phil. Mag.* **90** 1063

[43] Björkas C, Nordlund K and Dudarev S 2009 Modelling radiation effects using the *ab initio* based tungsten and vanadium potentials *Nucl. Instrum. Methods Phys. Res.* B **267** 3204–8

[44] Ziegler J F, Biersack J P and Littmark U 1985 *The Stopping and Range of Ions in Matter* (New York: Pergamon)

[45] Landolt–Börnstein 1991 *Numerical Data and Functional Relationships in Science and Technology: Refractory Metal Systems* (Berlin: Springer)

[46] Marinica M-C, Willaime F and Crocombette J-P 2012 Irradiation-induced formation of nanocrystallites with C15 Laves phase structure in BCC iron *Phys. Rev. Lett.* **108** 025501

[47] Giannozzi P *et al* 2009 QUANTUM ESPRESSO: a modular and open-source software project for quantum simulations of materials *J. Phys.: Condens. Matter* **21** 395502

[48] Becquart C S and Domain C 2007 *Ab initio* calculations about intrinsic point defects and He in W *Nucl. Instrum. Methods Phys. Res.* B **255** 23–6
[49] Becquart C S, Domain C, Sarkar U, DeBacker A and Hou M 2010 Microstructural evolution of irradiated tungsten: *ab initio* parameterisation of an OKMC model *J. Nucl. Mater.* **403** 75–88
[50] Muzyk M, Nguyen-Manh D, Kurzydłowski K J, Baluc N L and Dudarev S L 2011 Phase stability, point defects, and elastic properties in W–V and W–Ta alloys *Phys. Rev.* B **84** 104115
[51] Ventelon L, Willaime F, Fu C-C, Heran M and Ginoux I 2012 *Ab initio* investigation of radiation defects in tungsten: structure of self-interstitials and specificity of di-vacancies compared to other BCC transition metals *J. Nucl. Mater.* **425** 16–21
[52] Raouafi F, Barreteau C, Spanjaard D and Desjonquères M 2002 Stability of vicinal metal surfaces: from semi-empirical potentials to electronic structure calculations *Phys. Rev.* B **66** 045410
[53] Vitos L, Ruban A V, Skriver H L and Kollár J 1998 The surface energy of metals *Surf. Sci.* **411** 186202
[54] Van Zwol P, Derlet P M, Van Swygenhoven H and Dudarev S L 2007 BCC Fe surface and cluster magnetism using a magnetic potential *Surf. Sci.* **601** 3512–20
[55] Frederiksen S L and Jacobsen K W 2003 Density functional theory studies of screw dislocation core structures in BCC metals *Phil. Mag.* **83** 365
[56] Romaner L, Ambrosch-Draxl C and Pippan R 2010 Effect of rhenium on the dislocation core structure in tungsten *Phys. Rev. Lett.* **104** 195503
[57] Luo W, Roundy D, Cohen M L and Morris J W 2002 Ideal strength of BCC molybdenum and niobium *Phys. Rev.* B **66** 094110
[58] Chiesa S, Gilbert M R, Dudarev S L, Derlet P M and Van Swygenhoven H 2009 The non-degenerate core structure of a $\frac{1}{2}\langle 111\rangle$ screw dislocation in BCC transition metals modelled using Finnis–Sinclair potentials: the necessary and sufficient conditions *Phil. Mag.* **89** 3235
[59] Li H, Wurster S, Motz C, Romaner L, Ambrosch-Draxl C and Pippan R 2012 Dislocation-core symmetry and slip planes in tungsten alloys: *ab initio* calculations and microcantilever bending experiments *Acta Mater.* **60** 748
[60] Vitek V 1970 The core structure of $\frac{1}{2}\langle 111\rangle$ screw dislocations in b.c.c. crystals *Phil. Mag.* **21** 1049
[61] Duesbery M S, Vitek V and Bowes D K 1973 The effect of shear stress on the screw dislocation core structure in body-centered cubic lattices *Proc. R. Soc.* A **332** 85
[62] Clayton J D and Chung P W 2006 An atomistic-to-continuum framework for nonlinear crystal mechanics based on asymptotic homogenization *J. Mech. Phys. Solids* **54** 1604–39
[63] Henkelman G and Jonsson H 2000 Improved tangent estimate in the nudged elastic band method for finding minimum energy paths and saddle points *J. Chem. Phys.* **113** 9978
[64] Rodney D and Proville L 2009 Stress-dependent Peierls potential: influence on kink-pair activation *Phys. Rev.* B **79** 094108
[65] Garlick R G and Probst H B 1964 Investigation of room-temperature slip in zone-melted tungsten single crystals *Trans. AIME* **230** 1120
[66] Schadler H W 1960 Deformation behaviour of zone-melted tungsten single crystals *Trans. AIME* **218** 649
[67] Brunner D 2000 Comparison of flow-stress measurements on high-purity tungsten single crystals with the kink-pair theory *Mater. Trans. JIM* **41** 152
[68] Ventelon L, Willaime F and Leyronnas P 2009 Atomistic simulation of single kinks of screw dislocations in α-Fe *J. Nucl. Mater.* **386–388** 26
[69] Giannattasio A, Tanaka M, Joseph T D and Roberts S G 2007 An empirical correlation between temperature and activation energy for brittle-to-ductile transitions in single-phase materials *Phys. Scr.* **T128** 87–90
[70] Swinburne T, Dudarev S L, Fitzgerald S P, Gilbert M R and Sutton A P 2013 Theory and simulation of the diffusion of kinks on dislocations in BCC metals *Phys. Rev.* B **87** 064108
[71] Eshelby J D 1962 The interaction of kinks and elastic waves *Proc. R. Soc.* A **266** 222
[72] Proville L, Ventelon L and Rodney D 2013 Prediction of the kink-pair formation enthalpy on screw dislocation in α-iron by line tension model parametrized on empirical potentials and first principles calculation *Phys. Rev.* B **87** 144106
[73] Cereceda D, Stukowski A, Gilbert M R, Queyreau S, Ventelon L, Marinica M-C, Perlado J M and Marian J 2013 Assessment of interatomic potentials for atomistic analysis of static and dynamic properties of screw dislocations in W *J. Phys.: Condens. Matter* **25** 085702